Supplement of Atmos. Chem. Phys., 26, 6541–6556, 2026
https://doi.org/10.5194/acp-26-6541-2026-supplement

Atmospheric Chemistry and Physics
Open Access

Supplement of

Measurement report: Optical properties of carbonaceous aerosols modulated by source variations of spring haze

Yuan Cheng et al.

Correspondence to: Jiu-meng Liu (jiumengliu@hit.edu.cn)

Determination of $(b_{\mathrm{abs}})^*$ by AE33

When running AE33, the directly reported parameters were BC mass concentrations derived from the light absorption measurements in different channels, i.e., at different wavelengths:

$$\mathrm{BC_i} = \frac{(b_{\mathrm{abs}})_{\mathrm{i}}^{*}}{C_0 \times \mathrm{MAE_i}} \tag{1}$$

where $\mathrm{BC_i}$ indicates black carbon concentration reported for the ith channel; $(b_{\mathrm{abs}})_{\mathrm{i}}^{*}$ indicates the light absorption coefficient measured for the ith channel, which has been accounted for the loading effect using a compensation algorithm incorporated into the instrument; C_0 indicates the default correction factor (1.39) for the multiple scattering effect; $\mathrm{MAE_i}$ indicates the BC's mass absorption efficiency (i.e., mass absorption cross-section) assumed for the ith channel. The assumed MAE values are 18.47, 14.54, 13.14, 11.58, 10.35, 7.77 and 7.19 $\mathrm{m^2/g}$ for the seven channels which have measurement wavelengths of 370, 470, 520, 590, 660, 880 and 950 nm, respectively. Then using the constant C_0 and wavelength-resolved MAE, $(b_{\mathrm{abs}})^*$ could be calculated at various wavelengths using the following equation:

$$(b_{\mathrm{abs}})_{\mathrm{i}}^{*} = \mathrm{BC_i} \times C_0 \times \mathrm{MAE_i} \tag{2}$$

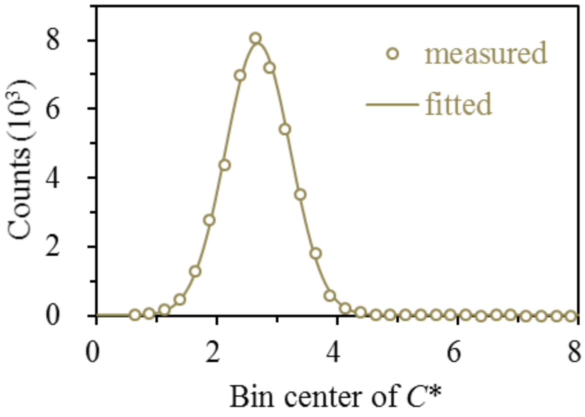

Figure S1. Distribution of C^*, i.e., the ratio of AE33-based $(b_{abs})^*$@880 to PAX-based b_{abs}@870. Here the C^* values were divided into 30 equal-width bins. Each bin had a width of 0.25, with C^* ranges of 0.50–0.75 and 7.75–8.00 (i.e., centers of 0.625 and 7.875) for the first and last bins, respectively. As shown by the solid line, the measured distribution of C^* could be fitted by a Gaussian function: $y = y_0 + A \times \exp[-(x-\mu)^2/(2\sigma^2)]$, where μ and σ are the mean and standard deviation of the distribution, respectively. Results involved in this figure were for the entire measurement period.

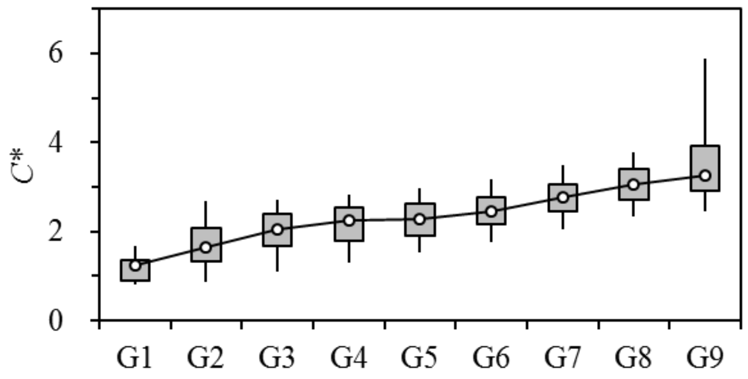

Figure S2. Comparison of C^* across various groups with increasing SSA levels. The first group (G1) had a SSA range of below 0.60, whereas the other 8 groups (G2 to G9) had the SSA ranges increasing from 0.60–0.65 to 0.95–1.00 with the same width of 0.05. Results involved in this figure were for the entire measurement period.

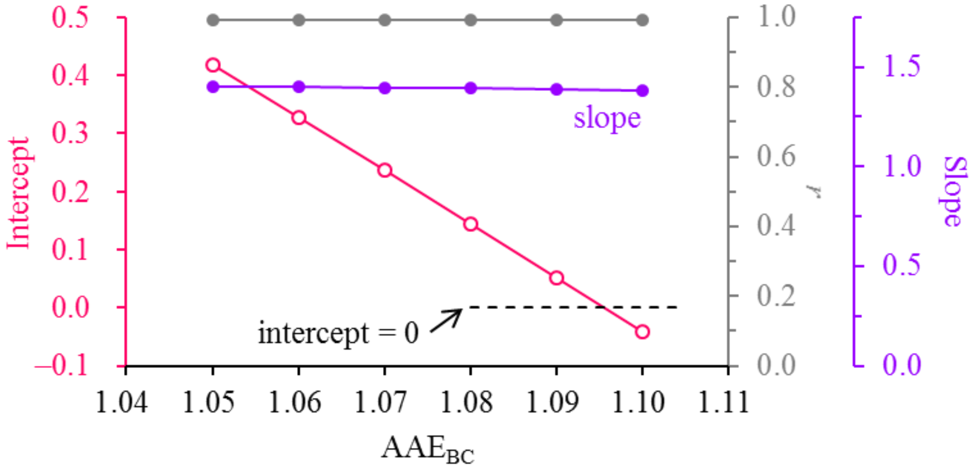

Figure S3. The same as Figure 4 in the main manuscript but for a narrowed AAE$_{BC}$ range of 1.05 to 1.10 (with a refined increment of 0.01).

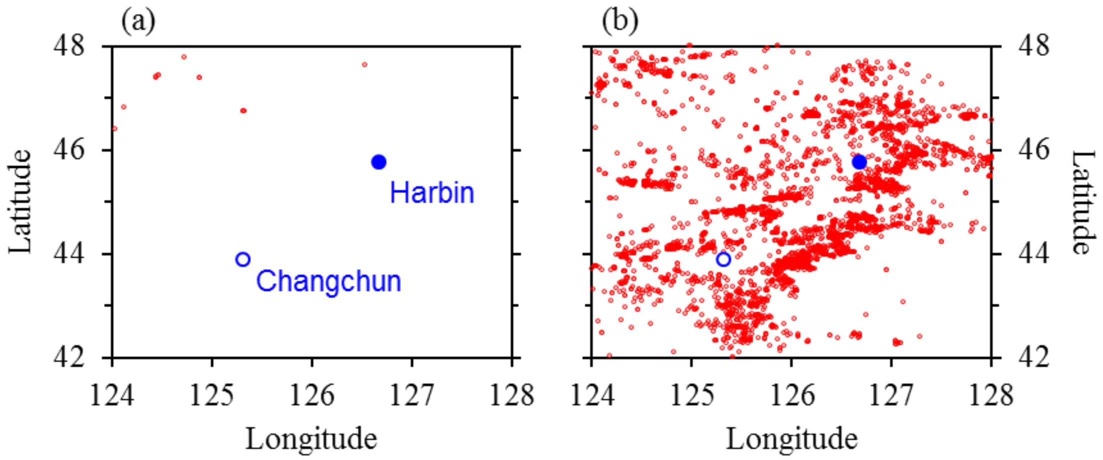

Figure S4. Cumulative fire hotspots detected during **(a)** April 28–29 and **(b)** April 1–2, 2023 around Harbin, with their locations shown by the red circles. These two periods were characterized by contrasting levels of K^+/sulfate, i.e., 0.03–0.07 and 0.41–0.55, respectively. The HC metropolitan area has two central cities as marked by the blue circles. The fire data were based on the joint NASA/NOAA Suomi National Polar-orbiting Partnership (S-NPP) satellite, and were downloaded from the Fire Information for Resource Management System (FIRMS; https://firms.modaps.eosdis.nasa.gov/).

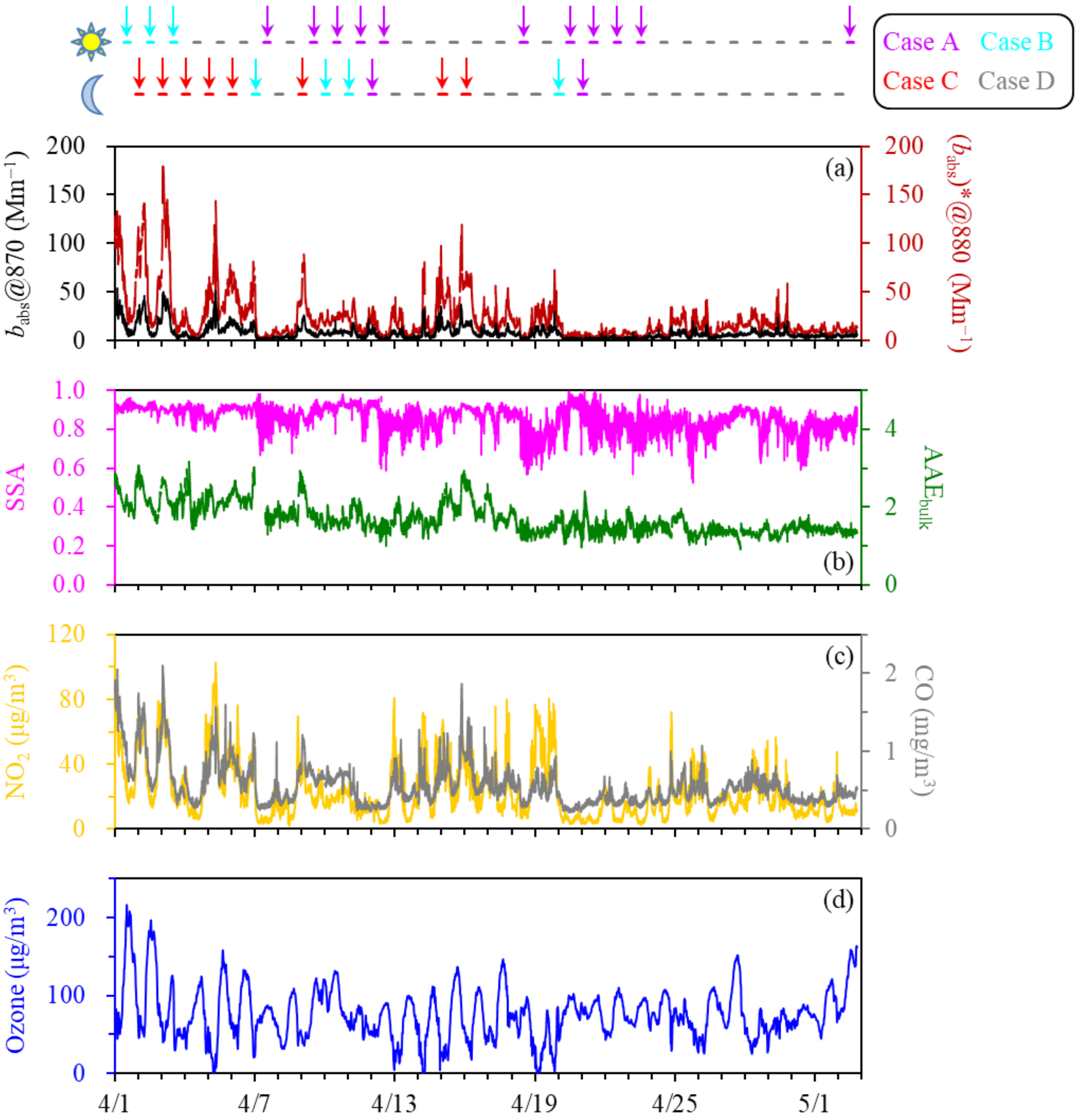

Figure S5. Distributions of the sampling segments for different groups of filter samples. Cases A to D correspond to the dust-impacted, fire&dust-impacted, fire-impacted and typical samples, respectively. The segments are color-coded by sample types, while for the distinct episodes (cases A to C), the samples in each group are also highlighted by the arrows. The sun and moon symbols indicate the daytime and nighttime samples, respectively. The on-line measurement results are also shown, with (a) for the PAX-based b_{abs} at 870 nm and the AE33-based $(b_{abs})^*$ at 880 nm, (b) for the PAX-based SSA and the AE33-based AAE$_{bulk}$, (c) for NO$_2$ and CO, and (d) for ozone.

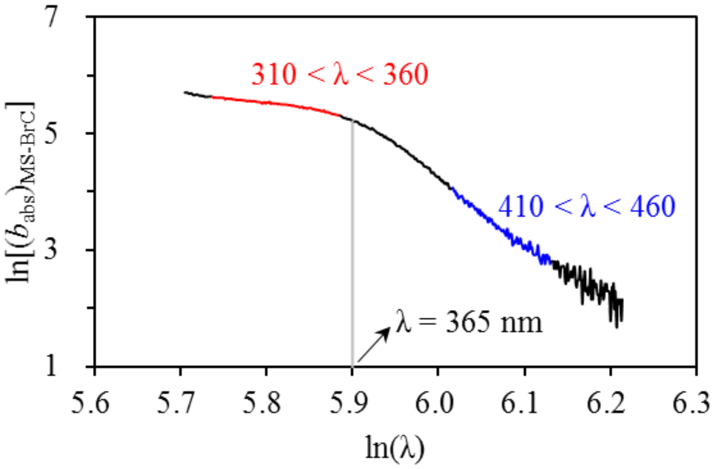

Figure S6. Light absorption spectrum measured for a fire-impacted sample collected on the night of April 1, 2023. The spectrum was non-linear due to the presence of a distinct absorption peak at ~365 nm, as shown by the vertical line. The non-linearity resulted in a higher AAE_{BrC} over 410–460 nm (as highlighted by the blue segment) compared to that over 310–360 nm (as highlighted by the red segment), i.e., higher $(AAE_{BrC})_{410\text{-}460}$ than $(AAE_{BrC})_{310\text{-}360}$. Thus, the non-linearity of the spectrum, i.e., the significance of the distinct peak at ~365 nm, could be estimated by ΔAAE_{BrC}, which was calculated as $(AAE_{BrC})_{410\text{-}460} - (AAE_{BrC})_{310\text{-}360}$.

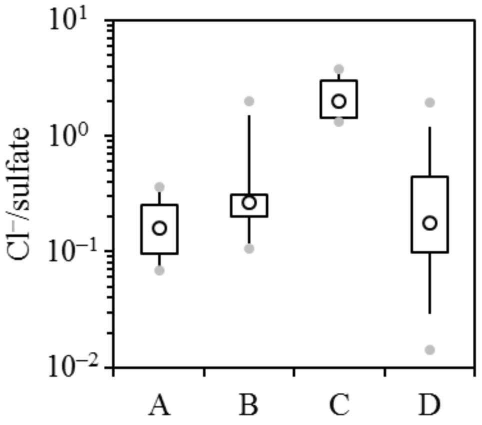

Figure S7. Variation of Cl^-/sulfate across cases of A–D, which correspond to the dust-impacted, fire&dust-impacted, fire-impacted and typical samples, respectively.

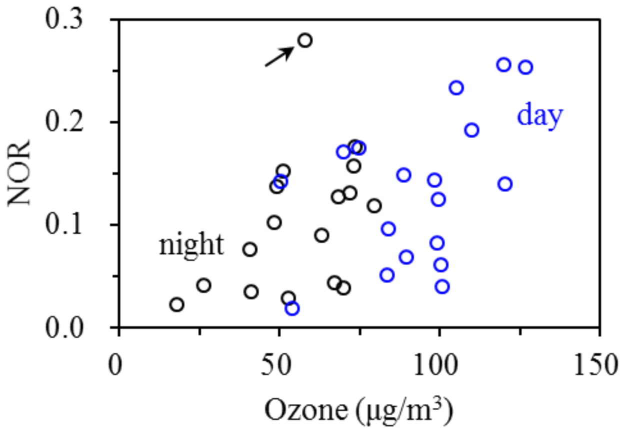

Figure S8. Relationship between NOR and ozone concentration for the typical samples. A total of 8 typical samples (including 6 nighttime ones and 2 daytime ones) experienced high RH levels of above 80%, whereas only one of them (collected on the night of April 27, 2023) showed an enhancement in NOR, as marked by the arrow. Thus the role of RH in nitrate formation should be limited for the typical samples.

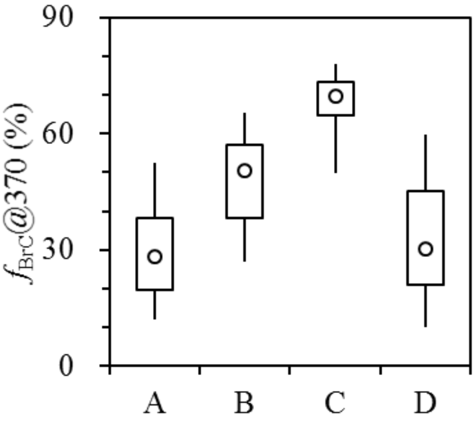

Figure S9. Comparison of f_{BrC}@370 across cases of A–D, which correspond to the dust-impacted, fire&dust-impacted, fire-impacted and typical samples, respectively.

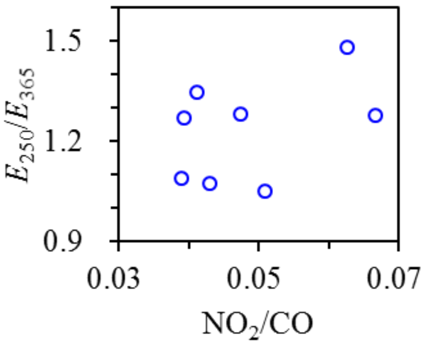

Figure S10. Dependence of E_{250}/E_{365} on NO_2/CO for the fire-impacted samples. To align with the off-line E_{250}/E_{365}, the time-resolved NO_2/CO were first averaged for the filter sampling segments and then used for the comparison.

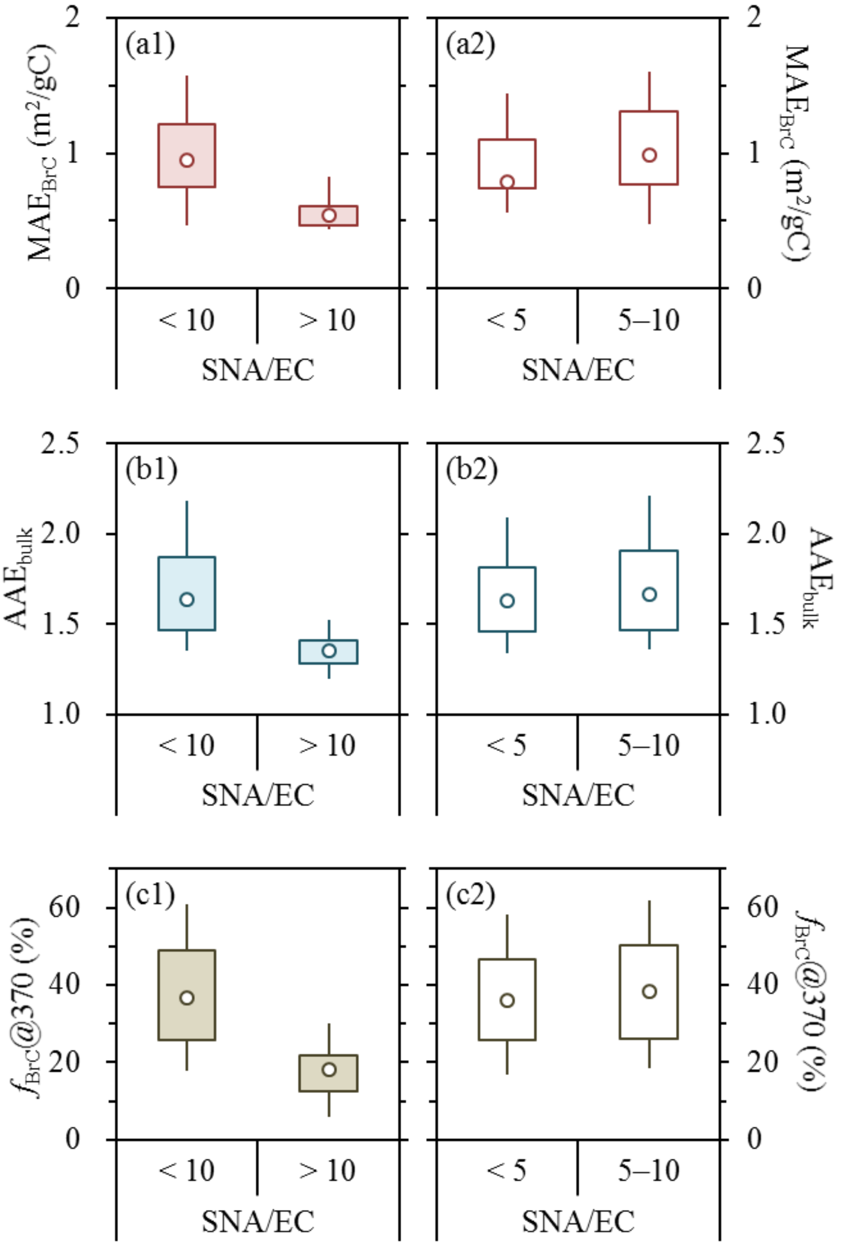

Figure S11. Comparisons of **(a1)** MAE$_{BrC}$, **(b1)** AAE$_{bulk}$, and **(c1)** f_{BrC}@370 with SNA/EC ratios of below and above 10, for the typical samples. The comparisons were also performed between the SNA/EC ranges of < 5 and 5–10, for **(a2)** MAE$_{BrC}$, **(b2)** AAE$_{bulk}$, and **(c2)** f_{BrC}@370. For the scenarios with SNA/EC < 10, no clear trend was observed for any parameter. Thus in the main manuscript, the typical samples with SNA/EC ratios of below 10 were not further distinguished when discussing the SOA impacts on BrC (section 3.4).

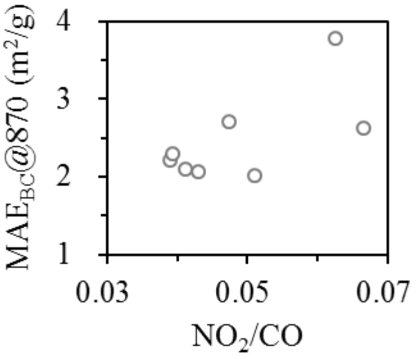

Figure S12. Dependence of MAE_{BC}@870 on NO_2/CO for the fire-impacted samples.